Journal of Materials Chemistry A

ROYAL SOCIETY OF CHEMISTRY

PAPER

View Article Online
View Journal | View Issue

Cite this: J. Mater. Chem. A, 2025, 13, 33749

Morphological insights into Se-driven charge transport and enhanced performance in $Sb_2(S,Se)_3$ solar cells

Yeeun Lee,†[a] Hongjae Shim,†[b] Mingrui He,†[b] Kaiwen Sun,[b] Mohammad Moein Seyfouri,[ac] Lei Wang,[a] Jan Seidel,[a] Chen Qian,*[b] Xiaojing Hao*[b] and Jae Sung Yun*[bd]

$Sb_2(S,Se)_3$ is a promising absorber for thin-film photovoltaics (PVs), yet its power conversion efficiency (PCE) remains limited. A key challenge lies in understanding the irregular grain morphology commonly found in these films, with their morphology-dependent electronic properties not being fully elucidated. Here, we investigate how Se incorporation alters grain structure and electronic properties in hydrothermally grown $Sb_2(S,Se)_3$ films. Selenium suppresses grain coalescence, yielding spherical-shaped grains (SGs) with increased grain boundary (GB) density. Kelvin probe force microscopy (KPFM) reveals enhanced charge separation at GBs and reduced trap-assisted recombination in Se-incorporated films. Stress simulations confirm that Se incorporation alleviates stress inhomogeneity. Nanoscale local *I–V* mapping indicates enhanced photocurrent near SGs, consistent with improved charge transport. Devices with Se-incorporated films achieve a PCE of 9.5% and FF of 65.5%. These findings demonstrate that moderate Se incorporation tailors microstructure and GB band structure, contributing to enhanced PV performance in $Sb_2(S,Se)_3$.

Received 7th July 2025
Accepted 1st September 2025

DOI: 10.1039/d5ta05469a

rsc.li/materials-a

Introduction

Antimony selenosulfide ($Sb_2(S,Se)_3$) has recently attracted increasing attention as a promising candidate for next-generation thin-film photovoltaics (PVs).[1–5] This material offers several advantages, including Restriction of Hazardous Substances (RoHS)-compliance, earth-abundant constituents, good thermal and chemical stability, and a tunable band gap ranging from 1.1 to 1.7 eV by adjusting the selenium-to-sulfur (Se/S) ratio.[3] However, its relatively low power conversion efficiency (PCE) remains a key obstacle to commercialization.

To address this limitation, prior studies have focused on optimizing fabrication techniques, such as deposition methods,[4,6–8] post-deposition treatments,[9,10] and the use of seeding layers.[11,12] In particular, hydrothermal deposition combined with post-annealing has recently enabled the fabrication of high-quality $Sb_2(S,Se)_3$ thin films, achieving PCEs exceeding 10.7%.[13] This approach allows for precise control over film growth, resulting in improved crystallinity and favorable grain orientations. Additionally, selenium incorporation into Sb_2S_3 has been shown to reduce deep-level defect densities while enabling optimal band gap tuning.[14,15]

Selenium incorporation also induces morphological modulation. In Sb_2S_3, post-annealing typically leads to a grain coalescence process, producing large, smooth grains.[7] In contrast, selenium-containing $Sb_2(S,Se)_3$ films exhibit much smaller grain sizes due to the suppression of this coalescence process, resulting in higher grain boundary (GB) density. The role of GBs in antimony chalcogenides has often been regarded as benign, owing to the absence of dangling bonds associated with their quasi-one-dimensional (Q1D) $(Sb_4(S,Se)_6)_n$ ribbon structure.[16] Nonetheless, the impact of GBs remains a subject of ongoing debate.

Recent studies have reported improved device performance in Sb_2S_3 films by increasing grain size through additive engineering.[17,18] Liu *et al.*[19] achieved a PCE increase from 6.0% to 7.1% by introducing Ce^{3+}, which promoted grain growth above 10 μm and reduced GB density from 1068 to 511 nm μm^{-2}. Similarly, Chen *et al.*[20] used monoethanolamine (MEA) to increase grain size to several micrometers, improving the PCE from 6.4% to 7.7%. These studies attributed enhanced carrier transport and collection to the formation of coalesced and smooth grains, suggesting a detrimental role of GBs.

[a]School of Materials Science and Engineering, University of New South Wales, Sydney, NSW 2052, Australia

[b]Australian Centre for Advanced Photovoltaics (ACAP), School of Photovoltaic and Renewable Energy Engineering, University of New South Wales, Sydney, NSW 2052, Australia. E-mail: c.qian@unsw.edu.au; xj.hao@unsw.edu.au

[c]X-Ray Facilities, Mark Wainwright Analytical Center, University of New South Wales, Sydney, NSW 2052, Australia

[d]School of Computer Science and Electronic Engineering, Advanced Technology Institute (ATI), University of Surrey, Guildford, Surrey GU2 7XH, UK. E-mail: j.yun@surrey.ac.uk

† These authors contributed equally to this work.

Conversely, high-performance Sb_2Se_3 devices often exhibit much smaller grain sizes, typically a few hundred nanometers.[21–24] This may be attributed to the fact that the optoelectronic properties of Sb_2Se_3 are more strongly dependent on grain orientation than on grain size. The effectiveness of GB engineering has been demonstrated by Chen *et al.*,[25] who achieved a PCE of 7.0% by inducing p-type inversion near GBs through $CuCl_2$ surface treatment, thereby enabling GBs to function as carrier transport pathways. Williams *et al.*[26] demonstrated, through density functional theory (DFT) simulations supported by scanning transmission electron microscopy (STEM), that GBs initially introduce gap states, but these are eliminated during structural relaxation. This work suggests that even GBs that disrupt covalent bonding and contain dangling bonds do not necessarily lead to increased carrier recombination.

While the role of GBs in Sb_2S_3 and Sb_2Se_3 has been explored separately, the impact of GBs in $Sb_2(S,Se)_3$ remains poorly understood. This gap in understanding could be a major barrier to achieving the commercialization-level PCE target of over 15% for $Sb_2(S,Se)_3$ devices.

In this work, we investigate how Se incorporation affects the grain structure and local electronic properties of $Sb_2(S,Se)_3$ thin films. In Se-free films, small amorphous grains in the precursor fully coalesce into large crystalline grains during post-annealing. In contrast, with Se incorporation, this coalescence is suppressed, resulting in smaller, spherical-shaped grains (SGs) with pronounced GBs that retain features of the precursor morphology. Using Kelvin probe force microscopy (KPFM), we reveal that GBs in these films induce downward band bending, a phenomenon previously reported to aid charge separation in materials such as lead halide perovskites and $Cu(In,Ga)Se_2$ (CIGS).[27–29]

To further understand the relationship between electronic structure and device performance, we conducted surface photovoltage (SPV) mapping and local *I–V* curve measurements to probe spatial variations in electrical behavior. In parallel, finite element simulations were used to evaluate stress distribution following annealing and to gain insights into the morphological differences between Sb_2S_3 and $Sb_2(S,Se)_3$. Our findings indicate that GBs between SGs promote effective charge separation and enhanced photocurrent generation. This mechanism is likely a significant contributor to the high performance 9.5% efficiency $Sb_2(S,Se)_3$ device.

Results and discussion

Sb_2S_3 and $Sb_2(S,Se)_3$ films were prepared using a hydrothermal process followed by post-annealing for crystallization. The samples are referred to as Se-free and Se-incorporated based on their estimated selenium content. X-ray diffraction (XRD) was conducted on films deposited on Glass/FTO/CdS substrates. As shown in Fig. 1a, the precursor films exhibit peaks near 24.8° and 28.2°, which correspond to the (100) and (101) planes of the underlying CdS, indicating that the precursors are largely amorphous. After annealing, new peaks corresponding to the crystallographic planes for $Sb_2(S_x,Se_{1-x})_3$, for Se-free and Se-incorporated films, respectively, emerge (Fig. 1b). A clear shift toward lower 2θ values is observed in the Se-incorporated film. This is attributed to the partial substitution of smaller S atoms (1.84 Å) with larger Se atoms (1.98 Å), which increases the average Sb–chalcogen bond length and causes the lattice expansion.[30] In our films, the (230) peak moves from 28.53° (Se-free) to 28.08° (Se-incorporated), corresponding to an ~1.5% increase in interplanar spacing. Similarly, the (211) and (221) peaks shift by ~0.41° and ~0.48°, respectively, toward lower angles, further confirming the structural expansion induced by selenium incorporation. The apparently less pronounced shift of the (130) and (230) peaks is due to their near coincidence with the CdS (100) and (101) peaks, which leads to partial peak overlap. In contrast, the Se-free film shows more separated peaks, particularly the (230) plane at 28.53°, which is distinctly shifted from the CdS (101) peak. These observations suggest that the Se-incorporated film experiences reduced lattice mismatch with CdS, possibly promoting more favorable nucleation at the CdS interface.[31]

Fig. 1c shows scanning electron microscope (SEM) images of the precursor films for both the Se-free and Se-incorporated samples, each exhibiting similar morphology and grain size. In contrast, the surface morphologies of final films for both samples in Fig. 1d show clear differences in grain evolution after post-deposition annealing at 350 °C for 10 min. The cross-sectional SEM images in Fig. S1 reveal comparable film thicknesses, suggesting that grain coalescence and growth occur preferentially in the lateral direction, where lateral mass transport plays a critical role in the grain coalescence kinetics.[32] In the Se-free film, post-annealing promotes grain coalescence, producing large and smooth grains, whereas the Se-incorporated film retains smaller grains, with sizes nearly identical to those in its precursor state. This observation contrasts with many chalcogenide-based PV systems such as $Cu_2ZnGe_xSn_{1-x}(S,Se)_4$, $Cu_2ZnSn(S,Se)_4$, and $Sb_2(S,Se)_3$ prepared *via* high-temperature post-selenization, in which increasing selenium content generally promotes grain growth.[33–36] In those cases, the enhanced grain growth has been attributed to the lower melting point, higher atomic mobility, and facilitated surface diffusion of selenium-rich compounds. However, several independent studies have also reported grain refinement in Se-incorporated $Sb_2(S,Se)_3$, consistent with our findings, indicating that the crystallization pathway is strongly dependent on the deposition technique.[7,37,38] In our hydrothermally grown and post-annealed films, selenium incorporation promotes preferential end-to-end stacking of quasi-one-dimensional $(Sb_4S(e)_6)_n$ ribbons, while the ribbon sides remain relatively inert due to van der Waals interactions. This structural anisotropy introduces van der Waals gaps that could confine atomic motion,[39] thereby hindering lateral coalescence and leading to the persistence of small, SGs in the Se-incorporated films. Energy-dispersive spectroscopy (EDS) results shown in Fig. S2 further confirm that a homogenous distribution of Se atoms with Se/S + Se ratio of 24.46%. The observed morphological difference arises from selenium-induced modifications of crystallization dynamics, rather than from compositional inhomogeneity. Furthermore, such

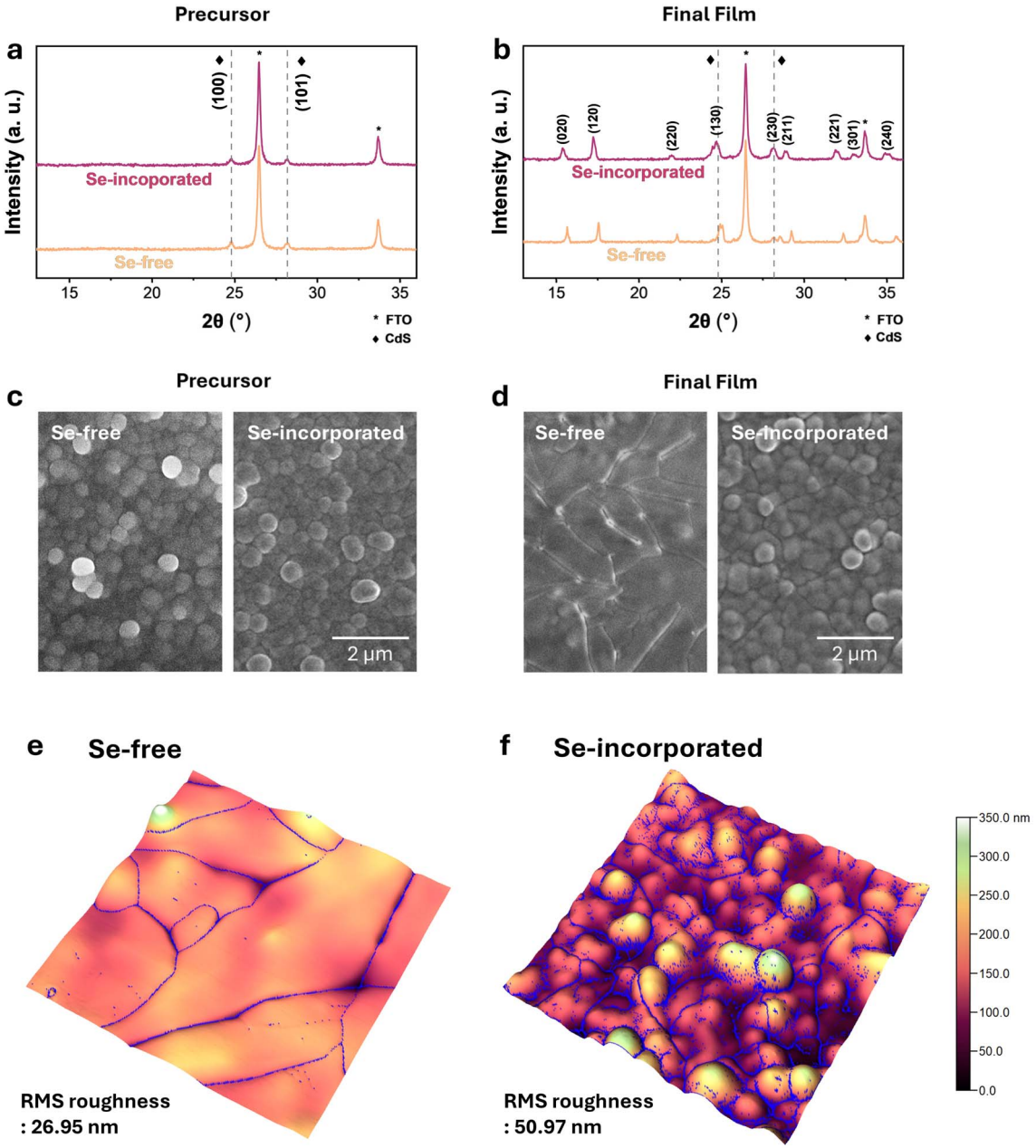

Fig. 1 (a and b) XRD patterns of Se-free and Se-incorporated films before and after post-annealing, respectively. Upon annealing, diffraction peaks corresponding to the (020), (120), (221), and (220) planes emerge. A shift toward lower 2θ values is observed in Se-incorporated, indicating lattice expansion due to Se incorporation. (c) SEM images of precursor films showing similar granular morphology. (d) SEM images after post-annealing reveal the formation of large, coalesced grains (CGs) in Se-free, while Se-incorporated maintains spherical-shaped grains (SGs) with visible necking. (e and f) AFM 3D topography of post-annealed Se-free and Se-incorporated films. The Se-incorporated film exhibits higher RMS roughness and GB density than Se-free.

uniform Se incorporation is expected to reduce the bandgap of $Sb_2(S,Se)_3$, as commonly reported for chalcogenide alloys,[14,30] which typically leads to enhanced light absorption and higher short-circuit current density (J_{SC}), accompanied by a trade-off of reduced open-circuit voltage (V_{OC}) due to the narrower bandgap.

To further analyze surface morphology, atomic force microscopy (AFM) was performed. The 3D topography images in Fig. 1e and f show that the Se-incorporated film has a significantly higher root-mean-square (RMS) roughness of 50.97 nm compared to 26.95 nm for Se-free one. Additional large-area scans (see Fig. S3) reveal that Se-free and Se-incorporated films have average grain sizes of 1.52 μm and 0.31 μm, respectively. The corresponding GB lengths are 121.6 μm and 306.6 μm in the same area, indicating more than double the GB density in Se-incorporated. Each film exhibits distinctive grain morphology: large, coalesced grains (CGs) are observed in the Se-free film, whereas the Se-incorporated film predominantly features SGs.

Representative topographic line profiles across selected GBs in the Se-free and Se-incorporated films are shown in Fig. 2a and e, respectively. In the Se-free film, the GBs are narrow and steep, while in the Se-incorporated film they are broader and exhibit more gradual profiles. This morphological difference is attributed to grain boundary grooves (GBGs), which form at the film surface where GBs intersect during annealing. GBGs arise to relieve the imbalance between GB energy and surface energy. We extracted the dihedral angle (φ) from linear fits of the topographic profiles across selected GBs (see Table S1). As shown in Fig. 2c and f, the Se-free film exhibits sharper GBGs between CGs, with $\varphi \approx 130°$, while the Se-incorporated film displayed shallower grooves between SGs, with $\varphi \approx 150°$.

Upon post-annealing process for the film re-crystallization, the GB area decreases to lower Gibbs free energy. The total Gibbs free energy change upon the GBG formation is[40,41]

$$\delta G = \gamma_{GB}\delta a - 2\gamma_s \cos\left(\frac{\varphi}{2}\right)\delta a$$

where γ_{GB} and γ_s are the GB energy and surface energy per unit area, respectively, φ is the dihedral angle at the groove root, and δa is the unit area removed at the GB–surface junction. The dihedral angle φ is directly related to the ratio of GB energy (γ_{GB}) to surface energy (γ_{GB}), following the relation:

$$\frac{\gamma_{GB}}{\gamma_s} = 2\cos\left(\frac{\varphi}{2}\right)$$

From this relation, a larger φ angle indicates a lower γ_{GB}/γ_s ratio, suggesting that the GB possesses relatively lower energy compared to the surface. Therefore, the broader and shallower GBGs observed in the Se-incorporated film (with $\varphi \approx 150°$) imply that the system has undergone more extensive energy minimization during annealing, reaching a more thermodynamically relaxed state. In contrast, the sharper grooves of GBs between CGs in the Se-free film ($\varphi \approx 130°$) reflect a larger imbalance between GB and surface energies of CGs, leading to more pronounced groove formation. This morphological evolution is consistent with the weak grain coalescence in Se-incorporated compared to in Se-free. The reduced extent of grain coalescence can be associated with intrinsically lower GB energy in Se-incorporated precursor film. In this case, the driving force for coalescence is weaker, allowing the small grains and their boundaries to remain stable during annealing. Such a reduction in γ_{GB} could arise from several factors, including a lower degree of grain misorientation or the presence of Se-related species that stabilize the GB energetically.

While morphology provides valuable insights, the electrical properties linked to the microstructure must also be considered to fully understand their impact on device performance. In particular, the influence of GBs can vary substantially depending on their crystallographic nature and the resulting surface potential landscape. To explore these factors, KPFM was employed to map the local potential distribution shaped by SG and CG structures in the Se-free and Se-incorporated films.

The corresponding CPD maps under dark conditions are shown in Fig. 2b for Se-free and Fig. 2d for Se-incorporated. The Se-incorporated film maintains more laterally uniform potential distribution compared to Se-free, as shown in the CPD

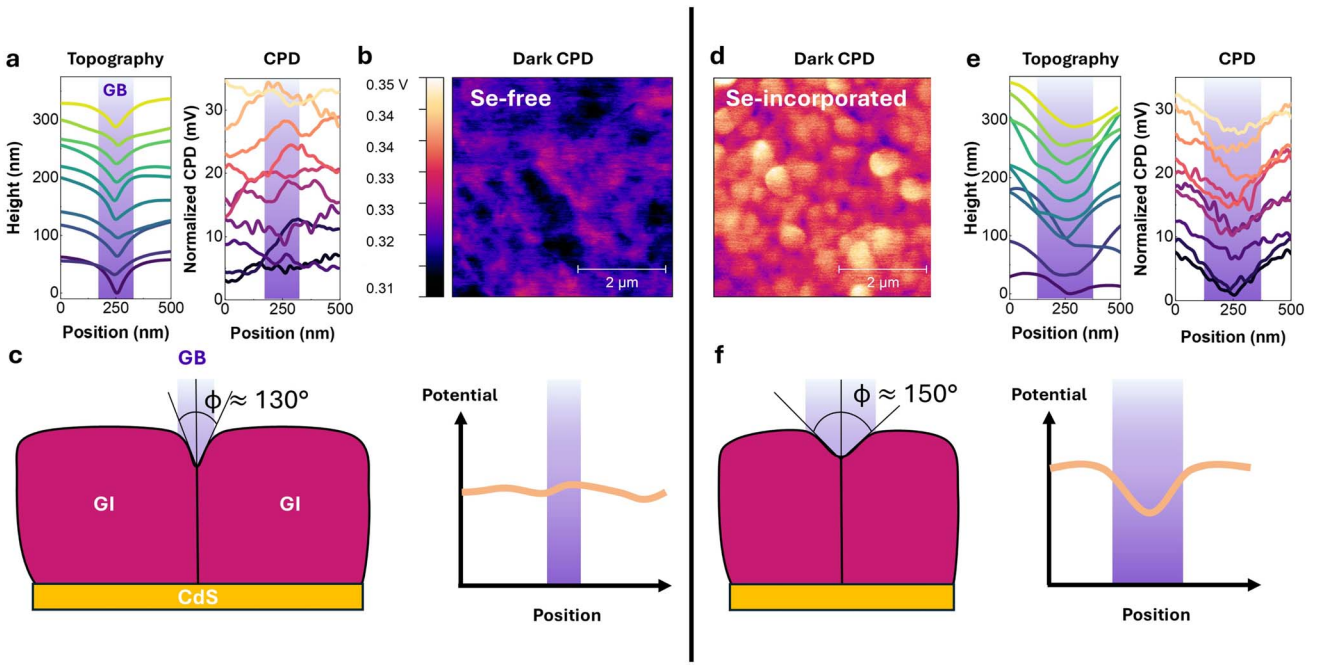

Fig. 2 (a and e) Representative topographic and contact potential difference (CPD) line profiles extracted across selected GBs in Se-free and Se-incorporated films (see Fig. S4), showing sharp GBGs in Se-free and more gradual grooves in Se-incorporated. (b and d) Corresponding CPD maps acquired under dark conditions, both presented with the same color scale range (0.31–0.35 V). (c and f) Schematic illustration of groove morphology and surface potential profiles at GBs for each case. The Se-incorporated film exhibits a stronger CPD drop at GBs and smoother groove profiles, suggesting downward band bending and improved potential continuity across grains.

histograms (Fig. S5 and Table S2). This suggests that although the local potential gradient at each GB is large, the overall electrostatic landscape across grains and GBs is more consistent. In contrast, the Se-free film shows greater inter-grain CPD variation and noticeable inhomogeneity within GIs, likely arising from electrically active intra-grain defects. Long-range lateral potential fluctuations can impede out-of-plane carrier transport, adversely affecting PV functionality.

In Se-free, the CPD at GBs is similar to or slightly higher than that in the grain interiors (GIs), suggesting flat or weak upward band bending. In contrast, the Se-incorporated film exhibits a notable reduction in CPD at GBs, indicating downward band bending. CPD line profiles across GBs and GIs, also shown in Fig. 2a and e, were analyzed statistically. The CPD gradually decreases toward the center of the GB, and this potential gradient extends along the GB over a length scale exceeding 100 nm. Box charts for the CPB at GB and GIs in the Se-free and Se-incorporated films are presented in Fig. S6. The Se-incorporated film shows a distinct CPD contrast between GBs and GIs by around, consistent with stronger downward band bending.

The impact of downward band bending on the optoelectronic properties of films is complex, as it depends heavily on the type and density of defects present at the GBs. In general, downward band bending at GBs attracts electrons and repels holes. If deep-level defect states for electrons exist, this band alignment can enhance non-radiative recombination. In contrast, GBs that are free of deep-level traps can promote the spatial separation of electrons and holes, thereby reducing the likelihood of recombination. In $Sb_2(S_x,Se_{1-x})_3$, which features a Q1D crystal structure, GBs that intersect along van der Waals planes, such as those between grains with (00*l*) orientations, are ideally free of dangling bonds and therefore unlikely to introduce bandgap states.[16] On the other hand, GBs that intersect covalent bonds, such as those between grains with (*hk*0) orientations, may induce deep-level defects. Accordingly, the influence of GBs exhibiting downward band bending on PV performance should be evaluated through their response under light illumination.

To investigate carrier dynamics under illumination, time-resolved KPFM (tr-KPFM) was performed on Se-free and Se-incorporated films deposited on Glass/FTO/CdS substrates. Full KPFM images are presented in Fig. S7 while these samples do not represent complete PV devices (*e.g.*, FTO/CdS/$Sb_2(S_x,Se_{1-x})_3$/spiro-OMeTAD/Au), the configuration mimics a functional junction under KPFM measurement conditions, allowing the extraction of SPV behavior as in working devices.[42,43] When illuminated, electron–hole pairs separate at the CdS/$Sb_2(S_x,Se_{1-x})_3$ junction. Electrons are drawn to the CdS layer, and holes accumulate at the top surface, which is subsequently measured by SPV. The measurement schematic and representative SPV maps under monochromatic illumination (405, 532, and 635 nm) are shown in Fig. 3a for the Se-free film and Fig. 3b for the Se-incorporated film.

In the Se-free film, illumination with 405 nm (blue) light leads to a CPD increase of approximately 270 mV. This indicates hole accumulation at the surface due to efficient electron extraction across the CdS/$Sb_2(S_x,Se_{1-x})_3$ interface. Once the light is turned off, the CPD quickly returns to the dark-state level, suggesting minimal charge trapping. Under green and red illumination, which penetrate deeper into the film closer to the CdS/Sb_2S_3 interface, the CPD continues to evolve even after the light is removed. This delayed decay, which lasts for more than 100 seconds, indicates slow recombination dynamics likely involving deep-level trap states located in the bulk or near the CdS interface. In contrast, the Se-incorporated film shows different behavior. For all excitation wavelengths, the CPD decreases gradually during illumination and returns rapidly to its initial state after the light is turned off. This behavior indicates a reduced involvement of trap states and suggests that the carrier dynamics are primarily governed by free carrier generation and recombination.

To further examine recombination dynamics, the CPD decay curves after turning off the blue, green, and red illumination were fitted with exponential decay functions, as shown in Fig. 3c and d. The extracted decay time constants (τ_1) were consistently higher in the Se-free film than in the Se-incorporated film, with the most pronounced difference observed under red illumination (6.07 ms and 2.65 ms for Se-free and Se-incorporated, respectively). This could be interpreted that recombination in the Se-free film is dominated by deep-level traps predominantly located within the bulk or at the CdS interface.[44] Overall, the rapid CPD relaxation observed in Se-incorporated indicates that the SPV response is primarily governed by free carrier separation, rather than trap-limited slower dynamics. In contrast, the Se-free film exhibits a significant SPV even under sub-bandgap IR excitation (~150 mV), further supporting that trap-assisted processes play a significant role in its SPV generation. Moreover, the absence of Se results in a wider bandgap in Se-free, which leads to a higher photovoltage under illumination and thus contributes to the overall SPV.

To visualize spatial variations, SPV maps were generated by subtracting the dark-state CPD from the illuminated-state CPD, as illustrated in Fig. 3e and f. In the Se-incorporated film (Fig. 3f), SPV is locally enhanced near the GBs of SGs, suggesting that downward band bending at GBs promotes carrier separation. Conversely, in the Se-free film (Fig. 3e), GBs show lower SPV compared to GIs, and the SPV distribution in grain interior is highly inhomogeneous, consistent with the potential fluctuations observed in the CPD maps obtained under dark conditions.

CPD maps measured under light illumination at different wavelengths (405, 532, 635, and 808 nm) for the Se-free and Se-incorporated devices are summarized in Fig. S8, and the corresponding SPV maps are presented in Fig. S9. Overall, the Se-free device exhibits lower SPV at GBs, whereas the Se-incorporated device shows enhanced SPV at GBs, regardless of the illumination wavelength. Notably, under infrared illumination (808 nm), where the photon energy is lower than the bandgap of the Se-free film, the CPD at the GBs is significantly higher than at the GIs. This suggests a higher concentration of photo-induced trapped holes or positive charges by states within bandgap. Furthermore, the CPD variation among CGs, as well as intra-grain CPD inhomogeneity, becomes more

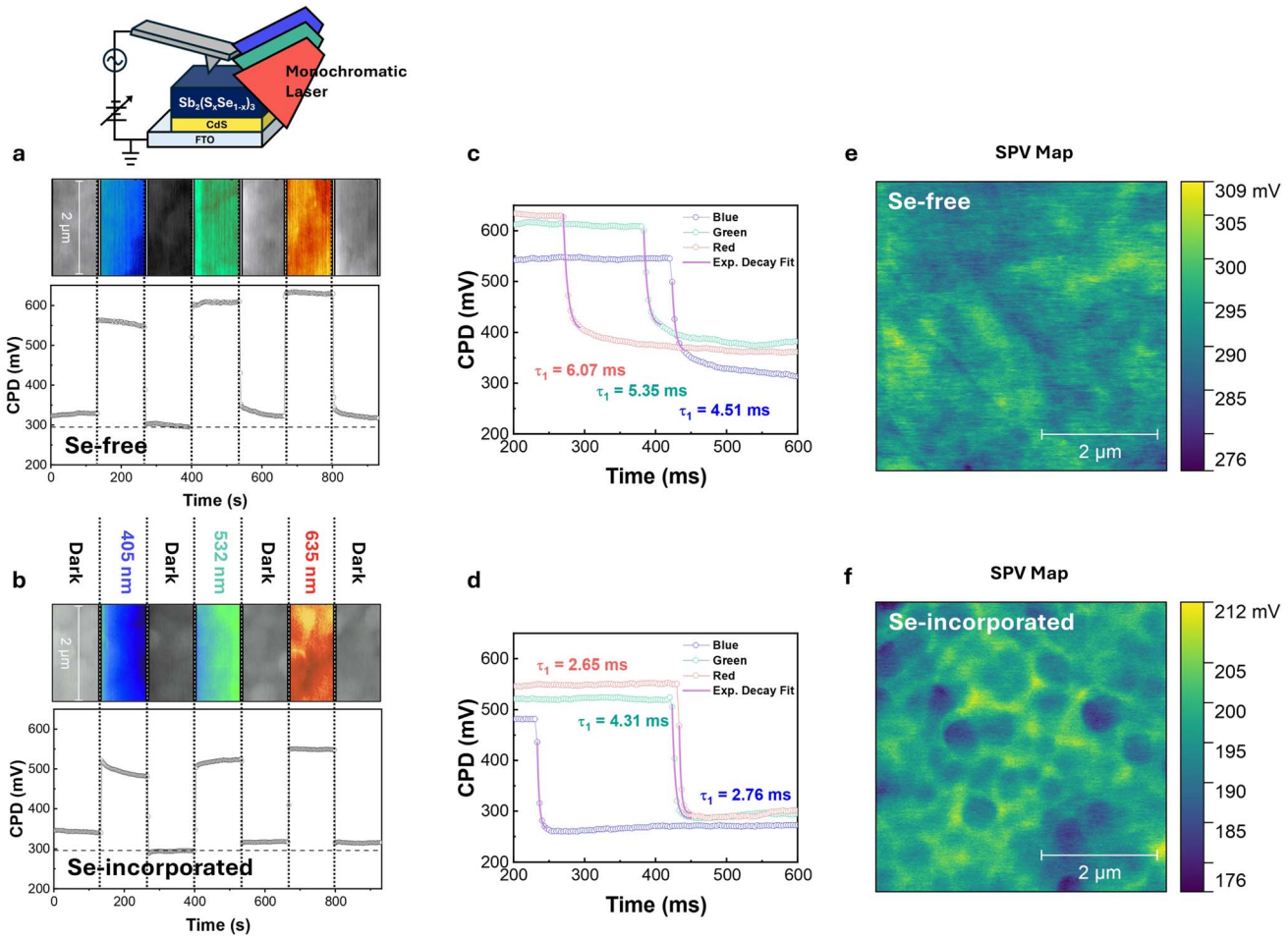

Fig. 3 (a and b) tr-KPFM maps and transient CPD responses under 405, 532, and 635 nm light for the (a) Se-free film and (b) Se-incorporated with device configuration and measurement schematic for tr-KPFM under monochromatic illumination. (c and d) CPD transients showing the decay of photoinduced CPD change after light-off under 405, 532, and 635 nm illumination for the (c) Se-free and (d) Se-incorporated films. The Se-free film exhibits slower CPD relaxation, particularly under red light, indicating trap-assisted recombination, while Se-incorporated shows faster recovery consistent with free carrier dynamics. (e and f) SPV maps obtained by subtracting dark CPD from illuminated CPD. Se-incorporated shows enhanced SPV near GBs of SGs, while Se-free shows reduced SPV at GBs and inhomogeneity within grain interiors.

pronounced under longer-wavelength illumination. These observations indicate that sub-gap states are predominantly localized at specific GBs, and that a high density of intra-grain defects is inhomogeneously distributed within the Se-free film. In contrast, the Se-incorporated device exhibits a reduced CPD at GBs under longer-wavelength illumination, suggesting minimal charge carrier trapping by sub-bandgap states. This behavior is associated with the benign nature of Sb_2Se_3 films,[16,25] attributed to Se-induced atomic relaxation at GBs,[26] which eliminates sub-bandgap states, as previously observed in Sb_2Se_3.

To further investigate the mechanical stress environment in the films, finite element simulations were performed using COMSOL to model the thermally induced stress distribution upon cooling from the post-annealing temperature of 350 °C. The simulation assumed a $Sb_2(S,Se)_3$ layer on pre-deposited CdS layer and the previously reported coefficient of thermal expansion (CTE) values of the materials were used.[45,46] Since the linear CTE of each axis of unit cell are different, the degree of thermal expansion varies depending on the crystal orientation of each grain.

3D von Mises stress maps for the films are presented in Fig. 4a and b, illustrating the higher grain-to-grain inhomogeneity in the stress in Se-free film after cooling. This could be attributed to the significant anisotropic CTE values of Sb_2S_3. The CTE along the b axis of unit cell (α_b) is over 13×10^{-6} K^{-1} while α_a and α_c are around 1.86×10^{-6} K^{-1} and 6.5×10^{-6} K^{-1}. Line profiles were extracted from stress maps (Fig. 4c and d) to enable more detailed analysis. Both Se-free and Se-incorporated films exhibit similar average stress levels around 450 MPa. Importantly, the Se-free film displays more pronounced grain-to-grain variation especially between (020) and (221) planes. These variations are spatially correlated with grain size and the anisotropic CTE of Sb_2S_3 and suggest that stress relief may not occur uniformly across the film, which could be correlated to the inhomogeneous surface potential grain-to-grain.

Fig. S10 and S11 present the depth-dependent stress distribution, indicating no discernible variation along the vertical

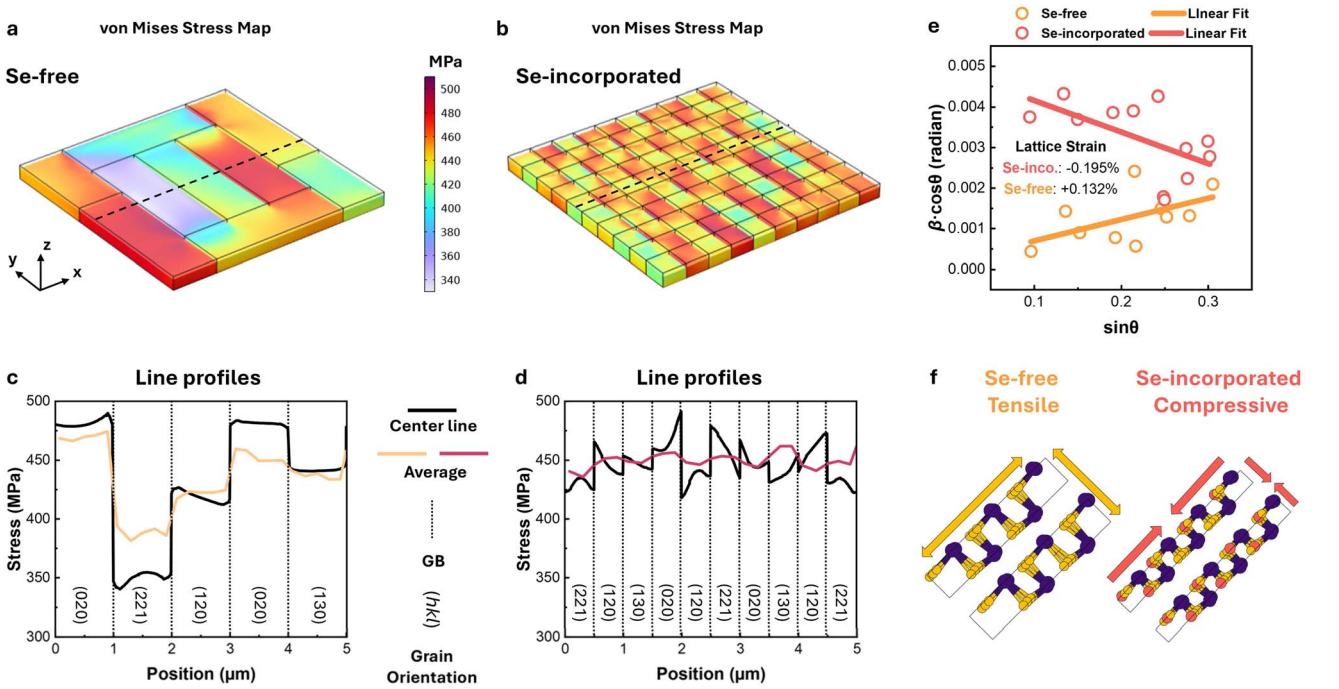

Fig. 4 (a and b) COMSOL-simulated 3D stress maps of the Se-free and Se-incorporated films after cooling from the 350 °C post-annealing process, assuming a CdS substrate. While the average stress is comparable, the Se-free film exhibits more severe grain-to-grain stress variation. (c and d) Line profiles extracted along the dashed lines in (a) and (b) with average lines. (e) WH plots extracted from the XRD patterns in Fig. 1a and b. (f) Schematic illustration of tensile and compressive lattice strain.

direction of the film. To further investigate possible depth-dependent structural changes, grazing-incidence wide-angle X-ray scattering (GIWAXS) measurements were performed on the Se-free and Se-incorporated films using incident angles (ω) of 0.1° and 1°, corresponding to surface-sensitive and bulk-sensitive probing depths, respectively. The GIWAXS patterns, shown in Fig. S12a and b, reveal no noticeable differences between the surface and bulk regions. Additionally, the in-plane and out-of-plane line profiles in Fig. S12c and d exhibit nearly identical peak positions, suggesting minimal variation in lattice strain throughout the film thickness.

Crystallographic strain states of the films were evaluated *via* Williamson–Hall (WH) analysis in Fig. 4e, revealing that the Se-free film exhibits a tensile strain of 0.132%, whereas the Se-incorporated film undergoes a compressive strain of 0.195%. Detailed information on the peak fitting, including peak positions and full width at half maximum (FWHM), is provided in Fig. S13, Tables S3 and S4. Previous studies have identified that antisite defects, particularly Sb atoms occupying S (Sb_S), can introduce deep electronic levels and act as detrimental recombination centers in $Sb_2(S,Se)_3$.[7,47,48] As illustrated in Fig. 4f, given the larger spatial requirement of Sb atoms in covalent bonding compared to S and Se, the formation of such antisites could be sterically hindered under compressive strain that reduces the available lattice space. A pertinent example can be found in a recent study on halide perovskites, where compressive strain was shown to increase the formation energy of interstitial defects. This effect is attributed to enhanced steric hindrance, which contributes to the suppression of their formation.[49] As supported by earlier XRD data, the Se-incorporated film exhibits (130) and (230) *d*-spacing values that closely match those of the underlying CdS (100) and (101) planes, indicating a reduced lattice mismatch. Conversely, the corresponding planes in the Se-0 film show a greater deviation from the CdS reference. This lattice mismatch can induce significant interfacial strain, which in turn promotes the formation of interfacial defects.

To comprehensively investigate the influence of SGs and their GBs on charge transport and PV performance, the film was analyzed by correlating morphology, local potential distribution, and short-circuit current (I_{SC}) using AFM, KPFM, and pointwise *I–V* mapping on the same region of the Se-incorporated film. In Fig. 5a–c and e, the 3D overlays, where the height represents topographical height, display the distributions of dark-state CPD, SPV, and I_{SC} over an identical area. We intentionally selected a region predominantly consisting of SGs and another region containing CGs, referred to as the SG region and CG region, respectively, for comparative analysis, as shown in Fig. 5a. As discussed previously, the GBs between SGs show broader and lower CPD compared to GIs (Fig. 5b), and these GBs also exhibit higher SPV (Fig. 5c). Some areas in the Se-incorporated film exhibit CG-like structures, although their grain size is much smaller than those in Se-free. In these regions, no significant SPV enhancement at GBs is observed.

To evaluate local electrical transport, pointwise *I–V* curves were acquired in contact mode across the scanned area, as schematically illustrated in Fig. 5d. This method minimizes topographical and crosstalk artifacts, which are often present in continuously scanned conductive-AFM (c-AFM) modes. Such

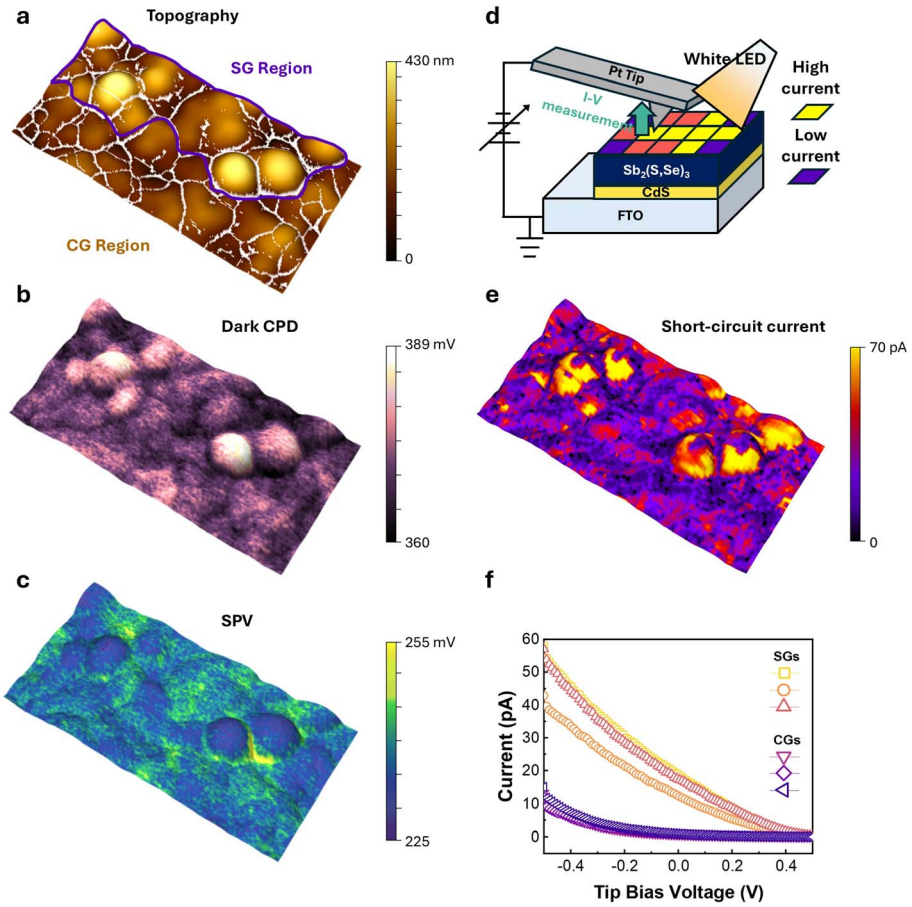

Fig. 5 Nanoscale and device-level PV performance analysis was conducted for Se-incorporated partial and full devices. 3D overlays where the height represents the surface topography, overlaid with (a) the AFM topography image, (b) the dark-state CPD map, (c) the SPV map, and (e) the short-circuit current map. (d) Schematic illustration of the *I–V* measurement setup. (f) Region-averaged *I–V* curves for SG and CG regions.

artifacts can introduce distortions, particularly in this study where regions with distinct morphologies are being compared. By measuring *I–V* characteristics at discrete points, the influence of surface roughness and tip–sample convolution is significantly reduced. I_{SC} values were extracted from the *I–V* curves and overlaid on the 3D topography as shown in Fig. 5e.

Notably, the *I–V* mapping with a Pt-coated AFM tip does not directly represent the real device behavior because the tip–sample interface forms a Schottky-type contact due to a work function mismatch. This additional barrier could lead to an underestimation of the V_{OC} and J_{SC} compared to devices employing HTL and Au electrodes. The increased contact resistance further lowers the FF, causing the measured *I–V* curves to appear more resistive in shape. The Pt-coated tip work function was calibrated against highly oriented pyrolytic graphite (HOPG, 4.50 eV (ref. 50)), yielding $\phi_{tip} = 4.864 \pm 0.053$ eV. From the measured CPD on the Se-incorporated film, the sample work function was determined to be $\phi_{sample} = 4.459 \pm 0.054$ eV, giving a tip–sample offset of 0.405 ± 0.009 eV. The Gaussian-fitted CPD histograms used for these extractions are provided in Fig. S14 and S15, and the corresponding averaged values with standard deviations are summarized in Table S5. This mismatch indicates the formation of a Schottky-type barrier at the tip/absorber interface, which is unfavorable for electron injection but relatively favorable for hole collection in the p-type $Sb_2(S,Se)_3$ absorber. Under illumination, such a barrier is dynamically modulated by photogenerated carriers, so the nanoscale *I–V* curves primarily reflect barrier-limited photocurrent flow rather than the intrinsic bulk conductivity. In this configuration, regions with relatively higher CPD values correspond to lower hole-injection barriers at the tip/absorber contact and thus support stronger local current flow, whereas lower CPD regions are less favorable for hole extraction. These effects imply that the absolute PV parameters extracted from Pt-tip *I–V* mapping cannot directly represent real device performance, although the technique still provides meaningful qualitative insight into the spatial distribution of current pathways across grains and GBs.

In contrast to the enhanced SPV at GBs (Fig. 3f and 5c), the I_{SC} at GBs is not notably higher and is in some cases lower than that of the surrounding GIs. In particular, the I_{SC} at the GIs of SGs is substantially higher than at GBs or within CGs. This observation is notable, as many c-AFM studies on other PV materials with beneficial GB effects typically report enhanced photocurrent at GBs. Importantly, the enhanced SPV is observed at GBs, whereas the photocurrent enhancement

appears predominantly within the GIs of SGs. This apparent discrepancy can be reconciled by recognizing that SPV probes charge separation under quasi open-circuit conditions, whereas point *I–V* mapping probes current flow under bias, which requires continuous, low-resistance pathways.[42] In Q1D $Sb_2(S,Se)_3$, weak van der Waals bonding at GBs increases the effective series resistance at the boundaries, thereby hindering vertical transport.[33] At the same time, downward band bending at GBs facilitates charge separation by attracting photoexcited electrons and repelling holes. Consequently, GBs primarily contribute to charge separation in their vicinity, whereas the vertical extraction and transport of these charges occurs preferentially through the GIs near GBs, where transport resistance is lower. This highlights the complementary roles of GBs in assisting local charge separation and GIs in sustaining efficient carrier transport.

To quantify this contrast, average *I–V* curves (Fig. 5f) were plotted for SG and CG regions extracted from the regions marked by white boxes in Fig. S16. The SG regions show significantly higher I_{SC} and V_{OC}. This enhancement may result from lower series resistance associated with the (*hk*1) orientation of SGs or reduced recombination enabled by favorable band alignment at GBs that supports charge separation.

To relate these nanoscale characteristics to overall device performance, solar cells with an identical structure of FTO/CdS/$Sb_2(S,Se)_3$/spiro-OMeTAD/Au (Fig. S17a) were fabricated using films with different Se contents. As shown in Fig. S17b, the Se-incorporated device exhibits higher fill factor (FF = 65.5%) and power conversion efficiency (PCE = 9.5%) than the Se-free device. The improved FF is consistent with nanoscale observations, where the interior of SGs near GBs demonstrates enhanced charge transport (Fig. 5e) and localized SPV response (Fig. 5c), both of which support more efficient charge extraction and reduced recombination losses.

The Se-free device exhibits a limited PCE of 5.5%, primarily due to a significant V_{OC} loss, indicating dominant non-radiative recombination. The external quantum efficiency (EQE) spectra of the Se-free and Se-incorporated devices are presented in Fig. S18. In the Se-incorporated device, the band edges are red-shifted, confirming the broadened spectral response after selenium incorporation. The J_{SC} values obtained by integrating EQE spectra are in good agreement with those measured from *J–V* curves, validating the accuracy of our device performance data. To decouple the influence of bandgap narrowing from improvement in photovoltage, we evaluated the V_{OC} deficit ($E_g/q - V_{OC}$). The optical bandgaps estimated from the EQE onset were ~1.62 eV for the Se-free device (766.9 nm) and ~1.41 eV for the Se-incorporated device (878.4 nm). Using the measured V_{OC} values of 0.691 V and 0.628 V, the corresponding V_{OC} deficits are ~0.93 V and ~0.78 V, respectively. Although the absolute V_{OC} decreases slightly upon Se incorporation, the reduction in V_{OC} deficit indicates that nonradiative recombination losses are effectively suppressed. This result, when considered together with the enhanced SPV at GBs and the increased photocurrent within grain interiors of the Se-incorporated film, suggests that deep-level defects at GBs as well as GIs are effectively passivated.

Our investigation suggests that this may originate from a high density of deep-level defects located at both GIs and GBs in the Se-free film. The formation of these defects is likely associated with inhomogeneous stress distribution, lattice mismatch with the underlying CdS layer, and tensile lattice strain. Since Se-free or low-Se-ratio devices are suitable for tandem applications with silicon PVs due to their wider bandgap, addressing these issues is essential for the practical implementation of $Sb_2(S_xSe_{1-x})_3$. One promising strategy is to introduce wide-bandgap materials (*e.g.* Sb_2O_3 or ZnS) at the GBs in Se-free films *via* surface treatment. By creating local energy barriers at GBs, such treatment may repel both electrons and holes from recombination-prone regions, thereby reducing the probability of non-radiative recombination associated with sub-bandgap states at GBs. Relevant examples include the incorporation of heavy alkali metals,[53] SnO_x,[54] and PbI_2 (ref. 55) at GBs in CIGS, $Cu_2ZnSn(S,Se)_4$, and halide perovskites, respectively.

Although the Se-incorporated device shows an extended spectral response, the EQE spectra also reveal reduced quantum efficiency in the short-wavelength region, which can be attributed to parasitic absorption in the underlying CdS buffer layer. Nevertheless, the choice of CdS plays a critical role in lattice matching, ribbon orientation, and mitigation of pinholes during $Sb_2(S,Se)_3$ film growth, which significantly influences the overall film quality.[51] This trade-off indicates that while CdS contributes to device stability and crystallinity, it simultaneously imposes a limitation on photocurrent collection. Furthermore, the relatively slow progress in PCE for $Sb_2(S,Se)_3$ devices compared with other chalcogenides is largely associated with the persistence of a high density of deep-level defects,[7] which continues to act as a bottleneck for further performance improvement. In addition, the lack of effective orientation control engineering remains a challenge, as many high-performance films still exhibit substantial lateral ribbon orientation,[52] thereby constraining out-of-plane charge transport pathways that predominantly govern PV performance. Looking forward, efficiency progress is likely to benefit from precise orientation control engineering, together with the rational selection of the underlying layer beneath $Sb_2(S,Se)_3$, to promote efficient charge transport and suppress parasitic absorption. These strategies could be effectively leveraged to further improve device performance. Additionally, strain engineering offers a route to suppress harmful defects. Incorporation of larger atomic radius elements into covalent bonding networks can generate compressive strain, which may raise the formation energy of detrimental defects such as Sb_S antisites. Since the *d*-spacings of the (130) and (230) planes in the film are smaller than those of the (100) and (101) planes in CdS, this approach can also reduce the lattice mismatch between the Se-free film and the CdS layer, thereby lowering the concentration of interface defects.

Conclusion

The results highlight that Se incorporation in $Sb_2(S,Se)_3$ thin films significantly alters grain morphology and GB

characteristics, which in turn govern local charge transport and device performance. The GBs in Se-incorporated film, featuring uncoalesced SGs, exhibits lower CPD than GIs, suggesting favorable downward band bending for carrier separation with suppressed recombination. Time-resolved KPFM reveals that Se-incorporated has reduced trap-related behavior compared to Se-free. SPV maps demonstrate enhanced charge separation at GBs between SGs in the Se-incorporated devices, whereas the Se-free devices exhibit reduced SPV at GBs. Furthermore, under sub-bandgap excitation, the SPV response in Se-free indicates a higher density of defect states within the bandgap localized at the GBs. COMSOL simulations indicate non-uniform stress across grains, with compressive lattice strain revealed by the WH plot in the Se-free film, suggesting a mechanically disadvantaged structure. Local *I–V* mapping confirms that SGs regions adjacent to GBs contribute to higher photocurrents, correlating with the superior FF (65.5%) and PCE (9.5%) observed in Se-incorporated devices. These findings demonstrate that appropriate Se incorporation modulates a microstructure that enhances charge separation and transport while suppressing deep-level defects.

Experimental section

Film and device fabrication

FTO-coated glasses (purchased from Liaoning Youxuan Tech. Co., Ltd) were pre-cleaned by deionized (DI) water, isopropanol, acetone, and ethanol (materials without specifically pointed out were all purchased from Sigma-Aldrich) for 10 min sequentially. UV ozone cleaner (Ossila, L2002A3) was employed to clean the FTO substrate before use. The cadmium sulfide layer was deposited on FTO substrate by the chemical bath deposition (CBD) method. Specifically, 11 mL $Cd(NO_3)_2$ (0.015 M), 7 mL thiourea (1.50 M) and 12 mL ammonia (1.56 M) were dissolved in 70 mL DI water. The deposition of CdS was conducted at 65 °C for 16 min with the substrate facing down in the growth solution.[1] Then $CdCl_2$ (20 mg in 1 mL methanol) was spin coated at 3000 rpm for 30 s and sample was heated at 400 °C for 10 min in air to improve the grain size of the CdS layer and incorporate Cl and O into the film.[56] This results in a better surface condition for epitaxial growth of $Sb_2(S,Se)_3$ in an autoclave reaction. After that, both Se-free and Se-incorporated absorber layers were deposited by the hydrothermal method. Specifically, 20 mm antimony potassium tartrate, 80 mm sodium thiosulfate tetrahydrate and 23 mg selenourea (99.97%, Alfa Aesar) were added sequentially into a Teflon autoclave (50 mL nominal volume) with 40 mL DI water (no selenourea for Se-free sample). The substrate inclined to the inside surface at 75°. Then the autoclave was sealed into a stainless-steel tank and heated in an oven (Across International, FO-19123) at 130 °C. The duration was 130 min for Se-incorporated sample and 180 min for Se-free sample. After natural cooling to room temperature, the samples were taken out and swilled with DI water and ethanol before being dried for 1 min in a vacuum dryer (Across International, AT-26) where the temperature was kept at 110 °C and the air pressure was 10 kPa. Afterward, the samples were transferred to a nitrogen-filled glove box and annealed at 350 °C for 10 min for crystallization. Subsequently, the spiro-OMeTAD was spin-coated at 3000 rpm for 30 s in a glovebox. The precursor solution was prepared by mixing 36.6 mg of spiro-OMeTAD powder (Lumitech), 14.5 μL of 4-*tert*butylpyridine (*t*BP), and 9.5 μL of a 520 mg per mL lithium trifluoromethanesulfonyl (Li-TFSI) together in acetonitrile in 1 mL of chlorobenzene. Finally, a gold anode was deposited by thermal evaporation under a pressure of 5×10^{-4} Pa.

Device characterization

J–V characteristics were determined using a Keithley 2400 apparatus under an AM 1.5 illumination with an intensity of 100 mW cm^{-2} provided by a standard xenon-lamp-based solar simulator (ABET Sun 3000 IV Tester). Before the test, the illumination intensity of a solar simulator was calibrated by a monocrystalline silicon reference cell (Oriel P/N 91150 V, with KG-5 visible color filter), previously standardized by the National Renewable Energy Laboratory (NREL).

XRD

XRD measurements were carried out using a PANalytical MPD system equipped with a copper (Cu) anode and a fast PIXcel detector. The system was calibrated before each scan to maintain angular precision. Samples were measured under ambient conditions to evaluate their crystalline structure.

To quantify lattice strain and crystallite size, WH analysis was performed based on multiple diffraction peaks. The FWHM values (β) of the diffraction peaks were plotted against $4\varepsilon \sin\theta$, following the WH equation:

$$\beta \cos\theta = \frac{k\lambda}{D} + 4\varepsilon \sin\theta$$

where θ is the Bragg angle, λ is the X-ray wavelength, D is the crystallite size, ε is the microstrain, and k is the Scherrer constant (taken as 0.9). The slope and intercept of the linear fit provide estimates of the microstrain and crystallite size, respectively. Detailed information on peak fitting and corresponding lattice parameters are presented in Fig. S13, Tables S3, and S4.

GIWAXS

GIWAXS measurements were conducted using a Rigaku SmartLab diffractometer equipped with a two-dimensional HyPix-3000 detector. To probe structural information at varying depths of the $Sb_2(S,Se)_3$ films, the incident angle (ω) was adjusted between 0.1° and 1.0°, enabling the investigation of both surface and subsurface regions.

COMSOL simulation

Finite-element (FEM) simulations were conducted using COMSOL Multiphysics (COMSOL, Inc.) to model the thermally induced stress distribution upon cooling from the post-annealing temperature of 350 °C to room temperature (25 °C). The modelled structure consisted of a $9 \times 9 \times 0.3$ μm^3 of $Sb_2(S,Se)_3$ layer modelled on a $9 \times 9 \times 0.06$ μm^3 CdS layer.

Grain geometries were idealized based on SEM and AFM topography images. Grains for the Se-free film were modeled with dimensions of $1 \times 3 \times 0.3$ μm^3, while the Se-incorporated film grains had dimensions of $0.5 \times 0.5 \times 0.3$ μm^3. To enhance the physical accuracy of the simulation, each grain was assigned specific crystal orientations selected among (020), (221), (120), and (130) planes. The thermal load was set to simulate linear cooling from an initial temperature of 350 °C to 25 °C over a period of 5 minutes.

Material properties including density, Young's modulus, Poisson's ratio, and CTE were obtained from the literature for the Se-free simulation, whereas properties for the Se-incorporated were determined by linear interpolation using literature values for Sb_2S_3 and Sb_2Se_3.[45,46,57] Orientation-dependent CTE values for each grain were calculated by projecting the general anisotropic CTE tensor along each grain's specific crystallographic orientation. These material properties are listed in Table S6. To evaluate the influence of residual stress generated during cooling, von Mises stress distributions were analyzed. The stress distribution was specifically assessed in a central $5 \times 5 \times 0.3$ μm^3 region within the film, excluding the outer 2 μm to avoid boundary artifacts and to accurately characterize intrinsic grain stress behavior.

AFM and KPFM

KPFM characterization was performed using an AIST-NT SmartSPM 1000 system in amplitude modulation mode. A Pt-coated AFM tip (HQ:NSC35/Pt, force constant ~5.4 N m^{-1}, resonance frequency ~150 kHz) was employed. All measurements were conducted within a nitrogen-filled chamber to prevent contamination and environmental interference. Prior to scanning, samples were purged with nitrogen gas. The tip–sample separation was maintained at ~40 nm for accurate surface potential measurements. An external monochromatic laser, positioned at a 30° angle, was used to uniformly illuminate the sample surface while minimizing shadowing by the probe. The wavelengths of the laser are 405, 532, 635, and 808 nm. The number of photons illuminated is 4.07×10^{15}. Scans were performed at a rate of 1.0 Hz. Multiple regions were analyzed for each sample to confirm the reproducibility and statistical relevance of the results.

Current–voltage mapping

The *I–V* mapping was performed using Cantilever D of the HQ:DPER-XSC11 AFM probe (TipsNano), which features a nominal spring constant of 42 N m^{-1} and a resonance frequency of ~350 kHz. The cantilever dimensions are 100 μm in length, 50 μm in width, and 2.7 μm in thickness. A ~15 nm platinum coating was applied uniformly across the cantilever surface, resulting in a tip radius of <20 nm. The conductive and chemically stable coating ensured consistent electrical contact during bias sweeps. These mechanical and geometric properties make Cantilever D well-suited for pointwise electrical measurements with high lateral resolution and mechanical stability. Measurements were performed in contact mode over a predefined scan area using a single-pass configuration. At each mapping point, the bias voltage was swept from −0.5 V to +0.5 V in 100 steps, with a dwell time of 2 ms per point. This pointwise approach minimizes topographical and crosstalk artifacts, allowing accurate assessment of local charge transport behavior. The measured resonance frequency and quality factor of the cantilever were ~344 kHz and ~491, respectively, with a nominal spring constant of 41.2 N m^{-1}.

Author contributions

Y. L., H. S., M. H., C. Q., and J. S. Y. conceived and validated the study. SEM and AFM measurements were conducted by Y. L. and H. S., with analysis performed by Y. L., H. S., M. H., J. S., and J. S. Y. XRD measurements were carried out by Y. L., H. S., and M. M. S. Device and film preparation, as well as device characterization, were performed by M. H. and C. Q. FEM simulations were conducted by Y. L., and analysis were conducted by Y. L., H. S., M. H., and J. S. Y. Visualization was prepared by Y. L., H. S., and J. S. Y. All authors, including K. S., and L. W., contributed to manuscript review and editing. Supervision was provided by C. Q., X. H., and J. S. Y.

Conflicts of interest

There are no conflicts of interest to declare.

Data availability

The data supporting this article are available in the SI, which includes additional detailed figures of materials characterization and device performance characterization, as well as supporting tables and notes. See DOI: **https://doi.org/10.1039/d5ta05469a**.

Acknowledgements

This work was supported by the Royal Society Research Grant (RGS/R1/221369) and the National Research Foundation of Korea (NRF) grant funded by the Korean government (MEST) (RS-2023-00257494 and 2022H1D3A2A01082324). Additional support was provided by the Australian Renewable Energy Agency (ARENA) as part of ARENA's Transformative Research Accelerating Commercialisation (TRAC) Program. M. H. acknowledges the Australian Centre for Advanced Photovoltaics as the recipient of an ACAP Fellowship, and X. H. acknowledges financial support from the ARC Future Fellowship (FT190100756). The Australian government does not accept responsibility for the views, information, or advice expressed herein.

References

1 C. Qian, K. Sun, J. Cong, H. Cai, J. Huang, C. Li, R. Cao, Z. Liu, M. Green, B. Hoex, T. Chen and X. Hao, *Adv. Mater.*, 2023, **35**, 2303936.
2 X. Wang, R. Tang, C. Jiang, W. Lian, H. Ju, G. Jiang, Z. Li, C. Zhu and T. Chen, *Adv. Energy Mater.*, 2020, **10**, 2002341.

3 C. Liu, S. Wu, Y. Gao, Y. Feng, X. Wang, Y. Xie, J. Zheng, H. Zhu, Z. Li, R. E. I. Schropp, K. Shen and Y. Mai, *Adv. Funct. Mater.*, 2022, **32**, 2209601.
4 C. Qian, J. Li, K. Sun, C. Jiang, J. Huang, R. Tang, M. Green, B. Hoex, T. Chen and X. Hao, *J. Mater. Chem. A*, 2022, **10**, 2835–2841.
5 L. Huang, J. Dong, Y. Hu, J. Yang, X. Peng, H. Wang, A. Liu, Y. Dong, H. Wang, C. Zhu, R. Tang, Y. Zhang and T. Chen, *Angew. Chem.*, 2024, **136**, e202406512.
6 X. Chen, B. Che, Y. Zhao, S. Wang, H. Li, J. Gong, G. Chen, T. Chen, X. Xiao and J. Li, *Adv. Energy Mater.*, 2023, **13**, 2300391.
7 R. Tang, X. Wang, W. Lian, J. Huang, Q. Wei, M. Huang, Y. Yin, C. Jiang, S. Yang, G. Xing, S. Chen, C. Zhu, X. Hao, M. A. Green and T. Chen, *Nat. Energy*, 2020, **5**, 587–595.
8 X. Wen, C. Chen, S. Lu, K. Li, R. Kondrotas, Y. Zhao, W. Chen, L. Gao, C. Wang, J. Zhang, G. Niu and J. Tang, *Nat. Commun.*, 2018, **9**, 2179.
9 J. Li, Z. Gao, X. Hu, S. Wang, Y. Liu, C. Wang, K. Dong, Z. Zeng, C. Tao and G. Fang, *Adv. Funct. Mater.*, 2023, **33**, 2211657.
10 Y. Zhao, S. Wang, C. Jiang, C. Li, P. Xiao, R. Tang, J. Gong, G. Chen, T. Chen, J. Li and X. Xiao, *Adv. Energy Mater.*, 2022, **12**, 2103015.
11 A. Amin, X. Duan, K. Zhao, K. Khawaja, W. Xiang, X. Qian and F. Yan, *Sol. RRL*, 2024, **8**, 2400151.
12 X. Pan, Y. Pan, L. Shen, L. Wang, R. Wang, G. Weng, J. Jiang, X. Hu, S. Chen, P. Yang, J. Chu and J. Tao, *Adv. Funct. Mater.*, 2023, **33**, 2214511.
13 M. A. Green, E. D. Dunlop, M. Yoshita, N. Kopidakis, K. Bothe, G. Siefer, X. Hao and J. Y. Jiang, *Prog. Photovolt.: Res. Appl.*, 2025, **33**, 3–15.
14 M. D. Khan, S. U. Awan, C. Zequine, C. Zhang, R. K. Gupta and N. Revaprasadu, *ACS Appl. Energy Mater.*, 2020, **3**, 1448–1460.
15 Y. Pan, X. Pan, R. Wang, X. Hu, S. Chen, J. Tao, P. Yang and J. Chu, *ACS Appl. Energy Mater.*, 2022, **5**, 7240–7248.
16 Y. Zhou, L. Wang, S. Chen, S. Qin, X. Liu, J. Chen, D.-J. Xue, M. Luo, Y. Cao, Y. Cheng, E. H. Sargent and J. Tang, *Nat. Photonics*, 2015, **9**, 409–415.
17 S. Chen, X. Wang, X. Chen, Y. Zhao, G. Dai, J. Yang, R. Tang, T. Chen, P. Hu and J. Li, *Adv. Funct. Mater.*, 2024, **34**, 2402978.
18 Z. Chen, X. Chen, J. Zhou, B. Tang, Y. Li, X. Yang and R. Zhou, *Energy Fuels*, 2024, **38**, 22536–22542.
19 X. Liu, Z. Cai, L. Wan, P. Xiao, B. Che, J. Yang, H. Niu, H. Wang, J. Zhu, Y. Huang, H. Zhu, S. J. Zelewski, T. Chen, R. L. Z. Hoye and R. Zhou, *Adv. Mater.*, 2024, **36**, 2305841.
20 X. Chen, X. Shu, J. Zhou, L. Wan, P. Xiao, Y. Fu, J. Ye, Y.-T. Huang, B. Yan, D. Xue, T. Chen, J. Chen, R. L. Z. Hoye and R. Zhou, *Light: Sci. Appl.*, 2024, **13**, 281.
21 G. Dai, X. Wang, S. Chen, X. Chen, B. Che, T. Chen, P. Hu and J. Li, *Adv. Funct. Mater.*, 2025, **35**, 2415215.
22 S. Rijal, D. Li, R. A. Awni, C. Xiao, S. S. Bista, M. K. Jamarkattel, M. J. Heben, C. Jiang, M. Al-Jassim, Z. Song and Y. Yan, *Adv. Funct. Mater.*, 2022, **32**, 2110032.
23 Z. Cao, B. Shao, Z. Ye, C. Liu, Z. Li, J. Dong, W. Wang, J. Li, H. Liu and Y. Zhang, *Adv. Funct. Mater.*, 2025, **35**, 2418974.
24 A. Amin, K. Zhao, K. Khawaja, Y. Wang, D. V. Pillai, Y. Zheng, L. Li, X. Qian and F. Yan, *ACS Appl. Mater. Interfaces*, 2025, **17**, 13814–13823.
25 C. Chen, K. Li, S. Chen, L. Wang, S. Lu, Y. Liu, D. Li, H. Song and J. Tang, *ACS Energy Lett.*, 2018, **3**, 2335–2341.
26 R. E. Williams, Q. M. Ramasse, K. P. McKenna, L. J. Phillips, P. J. Yates, O. S. Hutter, K. Durose, J. D. Major and B. G. Mendis, *ACS Appl. Mater. Interfaces*, 2020, **12**, 21730–21738.
27 C.-S. Jiang, R. Noufi, J. A. AbuShama, K. Ramanathan, H. R. Moutinho, J. Pankow and M. M. Al-Jassim, *Appl. Phys. Lett.*, 2004, **84**, 3477–3479.
28 C.-S. Jiang, R. Noufi, K. Ramanathan, J. A. AbuShama, H. R. Moutinho and M. M. Al-Jassim, *Appl. Phys. Lett.*, 2004, **85**, 2625–2627.
29 J. S. Yun, A. Ho-Baillie, S. Huang, S. H. Woo, Y. Heo, J. Seidel, F. Huang, Y.-B. Cheng and M. A. Green, *J. Phys. Chem. Lett.*, 2015, **6**, 875–880.
30 B. Yang, D.-J. Xue, M. Leng, J. Zhong, L. Wang, H. Song, Y. Zhou and J. Tang, *Sci. Rep.*, 2015, **5**, 10978.
31 X. Jin, Y. Fang, T. Salim, M. Feng, S. Hadke, S. W. Leow, T. C. Sum and L. H. Wong, *Adv. Funct. Mater.*, 2020, **30**, 2002887.
32 J. Jaseliunaite and A. Galdikas, *Materials*, 2020, **13**, 1051.
33 G. Lim, H. K. Park, Y. Wang, S. H. Ji, B. Shin and W. Jo, *J. Phys. Chem. Lett.*, 2024, **15**, 2825–2833.
34 D. B. Khadka and J. Kim, *J. Phys. Chem. C*, 2015, **119**, 1706–1713.
35 D. B. Khadka and J. Kim, *J. Alloys Compd.*, 2015, **638**, 103–108.
36 W. Wang, X. Wang, G. Chen, L. Yao, X. Huang, T. Chen, C. Zhu, S. Chen, Z. Huang and Y. Zhang, *Adv. Electron. Mater.*, 2019, **5**, 1800683.
37 R. Wang, D. Qin, S. Zheng, G. Weng, X. Hu, J. Tao, J. Chu, H. Akiyama and S. Chen, *Sol. Energy Mater. Sol. Cells*, 2023, **260**, 112501.
38 D. Qin, P. Yang, Y. Pan, Y. Wang, Y. Pan, G. Weng, X. Hu, J. Tao, J. Chu, H. Akiyama and S. Chen, *Sol. Energy Mater. Sol. Cells*, 2025, **280**, 113232.
39 C. Liu, X. Zou, Y. Lv, X. Liu, C. Ma, K. Li, Y. Liu, Y. Chai, L. Liao and J. He, *Nat. Nanotechnol.*, 2024, **19**, 448–454.
40 M. Hao, T. Duan, Z. Ma, M. Ju, J. A. Bennett, T. Liu, P. Guo and Y. Zhou, *Adv. Mater.*, 2023, **35**, 2211155.
41 M. Hao and Y. Zhou, *Joule*, 2024, **8**, 913–921.
42 H. Shim, A. S. Sharma, R. Mishra, J. Han, J. Lim, D. Zhang, Z. L. Teh, J. Park, J. Seidel, M. P. Nielsen, M. A. Green, S. Huang, J. S. Yun and J. Kim, *ACS Nano*, 2024, **18**, 31002–31013.
43 J. Lim, S. Lee, H. Shim, L. Wang, H. Cho, J. Kim, C. Cazorla, Y.-J. Kim, H. Min, M. Lee, X. Hao, S. R. P. Silva, J. Seidel, D. Kim, J. H. Noh and J. S. Yun, *Energy Environ. Sci.*, 2025, **18**, 5287–5297.
44 M. J. Choi, S. W. Lee, H. Shim, S. J. Shin, H. W. Chun, S. E. Yoon, J. A. Prayogo, J. Seidel, J. S. Yun, D. W. Chang and J. H. Kim, *Adv. Energy Mater.*, 2025, **15**, 2501113.

45 M. G. Herrmann, R. P. Stoffel, I. Sergueev, H.-C. Wille, O. Leupold, M. Ait Haddouch, G. Sala, D. L. Abernathy, J. Voigt, R. P. Hermann, R. Dronskowski and K. Friese, *Phys. Status Solidi B*, 2020, **257**, 2000063.
46 C. K. Gan, J. R. Soh and Y. Liu, *Phys. Rev. B: Condens. Matter Mater. Phys.*, 2015, **92**, 235202.
47 Z. Cai, C.-M. Dai and S. Chen, *Sol. RRL*, 2020, **4**, 1900503.
48 W. Lian, C. Jiang, Y. Yin, R. Tang, G. Li, L. Zhang, B. Che and T. Chen, *Nat. Commun.*, 2021, **12**, 3260.
49 C. Deger, S. Tan, K. N. Houk, Y. Yang and I. Yavuz, *Nano Res.*, 2022, **15**, 5746–5751.
50 W. N. Hansen and G. J. Hansen, *Surf. Sci.*, 2001, **481**, 172–184.
51 Y. Zeng, J. Huang, J. Li, K. Sun, U. A. Shah, H. Deng, X. Zhang, C. Sha, C. Qian, H. Song and X. Hao, *Sol. RRL*, 2022, **6**, 2200435.
52 Y. Zhao, X. Chen, J. Li and X. Xiao, *Sol. RRL*, 2023, **7**, 2300565.
53 T.-Y. Lin, I. Khatri, J. Matsuura, K. Shudo, W.-C. Huang, M. Sugiyama, C.-H. Lai and T. Nakada, *Nano Energy*, 2020, **68**, 104299.
54 K. Sardashti, R. Haight, T. Gokmen, W. Wang, L. Chang, D. B. Mitzi and A. C. Kummel, *Adv. Energy Mater.*, 2015, **5**, 1402180.
55 Q. Chen, H. Zhou, T.-B. Song, S. Luo, Z. Hong, H.-S. Duan, L. Dou, Y. Liu and Y. Yang, *Nano Lett.*, 2014, **14**, 4158–4163.
56 L. Wang, M. Luo, S. Qin, X. Liu, J. Chen, B. Yang, M. Leng, D.-J. Xue, Y. Zhou, L. Gao, H. Song and J. Tang, *Appl. Phys. Lett.*, 2015, **107**, 143902.
57 H. Koc, A. M. Mamedov, E. Deligoz and H. Ozisik, *Solid State Sci.*, 2012, **14**, 1211–1220.